Fronts and localized structures in a liquid-crystal-light-valve with optical feedback

S. Residori[a,*], A. Petrossian[b], T. Nagaya[c], C.S. Riera[d], M.G. Clerc[e]

[a] *Institut Non-Linéaire de Nice, UMR 6618 CNRS-UNSA, 1361 Route des Lucioles, 06560 Valbonne, France*
[b] *Laboratoire de Physique de l'ENS-Lyon, 46 Allée d'Italie, 69364 Lyon, France*
[c] *Department of Electrical and Electronic Engineering, Faculty of Engineering, Okayama University, Japan*
[d] *Harvard University, Pierce 409, 29 Oxford St., Cambridge, MA 02138, USA*
[e] *Departamento de Física, Facultad de Ciencias Físicas y Matemáticas, Universidad de Chile, Casilla 487-3, Santiago, Chile*

Abstract

We show that in a liquid-crystal-light-valve with optical feedback the Fréedericksz transition displays a subcritical character. Experimentally, we determine the extension of the bistable region and we study the propagation of fronts connecting the different metastable states. Theoretically, we derive an amplitude equation, valid close to the Fréedericksz transition point, which accounts for the subcritical character of the bifurcation. When, in the space of parameters, we move far from the Fréedericksz transition point, we adopt a mean-field model which is able to capture the qualitative features of all the successive branches of bistability. Close to the points of nascent bistability, by including diffraction effects we show the appearance of localized structures. Highly symmetric configurations of localized structures may be observed in the experiment by imposing a *N*-order rotation angle in the feedback loop. For increase of the input light intensity complex spatio-temporal dynamics arise, with either periodic or irregular oscillations in the position of the localized states. Rings dynamics is also observed, by the introduction of a small nonlocal shift in the feedback loop.

Keywords: Nonlinear optics; Pattern formation; Nonlinear dynamics

1. Introduction

Nonequilibrium processes often lead in nature to the formation of spatially periodic and extended structures, so-called patterns [1]. The birth of a pattern from a homogeneous state takes place through the spontaneous breaking of one or more of the symmetries characterizing the system [2]. In some cases, it is possible to localize a pattern in a particular region of the available space, so that we deal with localized instead of extended structures. From a theoretical point of view, localized structures in out of equilibrium systems can be seen as a sort of dissipative solitons [3]. Experimentally, during the last years localized patterns or isolated states have been observed in many different fields. Examples are domains in magnetic materials [4], chiral

* Corresponding author. Tel.: +33 4 92 96 73 17; fax: +33 4 93 65 25 17.
E-mail address: residori@inln.cnrs.fr (S. Residori).

bubbles in liquid crystals [5], current filaments in gas discharge experiments [6], spots in chemical reactions [7], oscillations in granular media [8], localized fluid states in surface waves [9] and in thermal convection [10], solitary waves in nonlinear optics [11–18]. All these localized states can be considered to belong to the same general class of localized structures, that is, they are patterns that extend only over a small portion of a spatially extended system. The mechanisms of localization of spatial structures rely on two main ingredients: the bistability, either between two homogeneous states or between a homogeneous state and a spatially periodic one, and the existence of an intrinsic spatial length, that is necessary to stabilize a localized state and which determines its typical size [19].

In optics, solitary waves have first been predicted to appear in bistable ring cavities [11]. Then, localized states have been largely studied not only for their fundamental properties but also in view of their potential applications in photonics [20–23]. The liquid-crystal-light-valve (LCLV) with optical feedback, as it was originally designed by the Akhmanov group [24], has been proved to be a suitable system for the observation and the study of localized structures [12–15]. Recently, we have proposed a Lifshitz normal form equation that describes the appearance of localized structures in the LCLV system [25]. Here, the bistability between homogenous states results from the subcritical character of the Fréedericksz transition, when the local electric field, which applies to the liquid crystals, depends on the liquid crystal reorientation angle [26,27]. Then, the simultaneous presence of bistability and pattern forming diffractive feedback assures the conditions for the appearance of localized structures.

Close to the point of Fréedericksz transition, the subcritical character of the bifurcation can be described by an amplitude equation derived from the Frank free energy of the liquid crystal [26,27]. Far from Fréedericksz transition, a mean-field model accounts for the appearance of successive branches of bistability [25]. In the space of parameters, the points of nascent bistability are identified as the locations where the surface of stationary states becomes s-shaped. Then, the Lifshitz normal form equation accounts for the appearance of another branch of solutions, corresponding to a spatially periodic state, giving rise to localized structures [25,28].

As a consequence of the nonvariational character of the LCLV system, it is generically expected that localized structures show permanent dynamics, such as propagation and oscillations of their positions [28]. Indeed, it is known that nonvariational effects are responsible of the permanent dynamics observed in extended patterns, such as the phase turbulence [29], the propagation of Ising–Bloch walls, predicted in oscillatory media [30] and observed in liquid crystal experiments [31], and the rotation of spirals observed in excitable media [35]. In the experiment, we observe a complex spatio-temporal dynamics of localized structures.

In this article, we present the LCLV experiment and the subcritical character of the Fréedericksz transition in the presence of optical feedback. A brief introduction to Fréedericksz transition is given in Section 2. Then, we outline the main mechanisms for the stabilization of the localized structures and we present their dynamical behaviours. The experiment is described in Section 3. In Section 4we present the subcritical Fréedericksz transition and in Section 5 the propagation of fronts. The theoretical model is presented in Section 6, where we derive an amplitude equation which is valid close to the Fréedericksz transition point. Sections 7 and 8 are devoted to the experimental characterization of localized structures and their dynamics. Finally, in Section 9 we present a theoretical approach, based on a mean-field approximation, which is able to capture the essential features of the system dynamics for all the successive branches of bistability far beyond the Fréedericksz transition point. Section 10 are the conclusions.

2. General features of the Fréedericksz transition

Liquid crystal materials are composed of anisotropic-shaped organic molecules. This results in the anisotropy of all their physical properties, like the dielectric and the magnetic susceptibility [32]. Most of the more popular liquid crystals are composed of molecules that are strongly elongated in one direction, so that they appear as a collection of rod-like molecules. In the isotropic phase the axis of the molecules are randomly distributed whereas in the nematic phase, the configuration of lowest energy is reached when all the molecules are, on average, aligned along a single direction, pointed out by the director $\vec{n}$. This long-range orientational order is a distinctive feature of nematic liquid crystals. The liquid

crystals we are going to consider in the following are always in the nematic phase, the temperature for the isotropic to nematic phase transition being $\sim$35 degC for our samples.

The nematic director, having the symmetry $\vec{n} \leftrightarrow -\vec{n}$, identifies a direction that can be experimentally specified either by applying an external field, like an electric or magnetic one, or by imposing some particular boundary conditions at the confining surfaces of the sample, that are the *anchoring* conditions. When two of these constraints are competing, the long-range orientational order may be partially destroyed.

The Fréedericksz transition is the elastic distortion of a nematic liquid crystal film under the action of a magnetic or electric field [33]. We will consider here the action of an electric field, but similar considerations and results can be obtained by substituting the electric field with a magnetic field and the dielectric tensor with the magnetic susceptibility. For a sufficiently high magnitude of the applied field, the initial alignment due to the anchoring conditions changes and, in the bulk of the sample, the system exhibits a reorientation of the nematic director, the so-called Fréedericksz transition [33,32]. The chosen geometry, that is, the orientation of the anchoring direction with respect to the externally applied field, determines the kind of elastic distortion that appears in the medium at the onset of the transition.

The Fréedericksz transition is usually associated to a supercritical bifurcation for the value of the reorientation angle inside the liquid crystal volume. The possibility of modifying the Fréedericksz transition into a first-order one was first considered in [34], where several theoretical predictions were given on the associated spatial effects. In the LCLV with optical feedback these spatial effects, like the propagation of fronts connecting differently oriented states, have been demonstrated experimentally [26,27].

3. Description of the experiment

The experiment, as shown in Fig. 1, consists of a LCLV with optical feedback. The LCLV is composed of a nematic liquid crystal film sandwiched in between a glass window and a photoconductive plate over which a dielectric mirror is deposed. Coating of the bounding surfaces induces a planar anchoring of the liquid crystal film (nematic director $\vec{n}$ parallel to the walls). Transparent electrodes covering the two confining plates permit the application of an electric field across the liquid crystal layer. The photoconductor behaves like a variable resistance, which decreases for increasing illumination. The feedback is obtained by sending back onto the photoconductor the light which has passed through the liquid-crystal layer and has been reflected by the dielectric mirror. The light beam experiences a phase shift which depends on the liquid crystal reorientation and, on its turn, modulates the effective voltage that locally applies to the liquid crystal layer. Thus, a feedback is established between the liquid crystal reorientation and the local electric field.

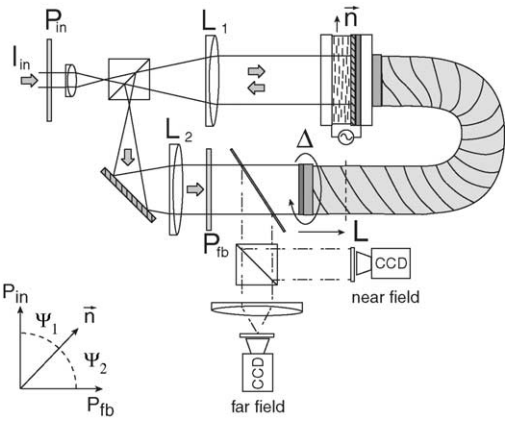

Fig. 1. Experimental setup: the LCLV is illuminated by a plane wave; the wave, reflected by the mirror of the LCLV, is sent back to the photoconductor through the optical fiber bundle. Δ is the angle of rotation of the fiber with respect to the front side of the LCLV. $\vec{n}$ is the liquid crystal nematic director; $P_{\rm in}$ and $P_{\rm fb}$ are the input and feedback polarizers; L_1 and L_2 are two confocal 25 cm focal length lenses and L is the free propagation length.

The feedback loop is closed by an optical fiber bundle and is designed in such a way that diffraction and polarization interference may be simultaneously present [12]. The free end of the fiber bundle is mounted on a precision rotation stage, which allows to fix a feedback rotation rotation angle Δ with a precision of ± 0.01 deg.

Diffraction is due to the optical free propagation length L. This last one can be varied from $L = 0$ to ± 20 cm and it is either positive or negative with respect to the plane on which a 1:1 image of the front side of the LCLV is formed (dashed line in Fig. 1). At the linear stage for the pattern formation, a positive (negative) L selects the first unstable branch of the marginal stability

curve as for a defocusing (focusing) medium [36,37]. The corresponding unstable wave numbers are, respectively

$$q_1 = \sqrt{3}\pi\sqrt{\frac{2}{\lambda|L|}}, \quad L > 0$$

and

$$q_0 = \pi\sqrt{\frac{2}{\lambda|L|}}, \quad L < 0.$$

The polarization interference is realized by fixing the angles ψ_1 and ψ_2 that the input and feedback polarizers form with to the liquid crystal director (see the left bottom of Fig. 1). In most of the experiments, ψ_1 and ψ_2 are fixed to 45 deg and -45 deg, respectively. For this condition, the system displays successive branches of bistability, either between two homogeneous and differently oriented states ($L = 0$), or between a homogeneous state and a periodic pattern ($L \neq 0$).

The total incident intensity is $I_{\text{in}} = 0.90\,\text{mW/cm}^2$. A 50% beam splitter is positioned before the LCLV, so that the intensity of the feedback light beam is limited to 25% of the total incoming intensity. This condition ensures that the LCLV works only around the switch-up point of his bistable response. The input beam has a Gaussian profile with a transverse size of approximately 2 cm, whereas a diaphragm before the fiber bundle selects a central active zone with a diameter of 1.2 cm.

The Fréedericksz transition point is attained for an applied voltage V_0 of approximately $3V_{\text{rms}}$ with a frequency of 5 kHz [26]. By increasing V_0, successive branches of bistability are observed. Most of the experimental observations here reported were obtained either close to the Fréedericksz transition point, $V_0 \simeq 3.2V_{\text{rms}}$, or close to the bistable branch located around $V_0 = 18.5V_{\text{rms}}$. For this high value of the applied voltage, the reoriented liquid crystal sample becomes similar to an homeotropic one (nematic director $\vec{n}$ perpendicular to the confining walls). Thus, the equilibrium state of the reoriented sample is close to saturation of the response, because the nematic director is almost aligned with the applied electric field. In this almost saturated regime, the system becomes much less sensitive to external perturbations, coming from noise sources or inhomogeneities of the LCLV.

In both cases, either close to $V_0 = 18.5V_{\text{rms}}$ or close to the Fréedericksz transition point, the LCLV works around a point of nascent bistability, where it may be assimilated to a phase slice with a step-like response [38].

4. Subcritical Fréedericksz transition

In general, the equation for the phase shift induced by the liquid crystal reorientation, $\varphi = \varphi(x, y, t)$, can be written as [12]

$$\frac{\partial\varphi}{\partial t} = -\frac{\varphi - \varphi_0}{\tau} + D\nabla_\perp^2\varphi + \alpha I_w(x, y, t), \tag{1}$$

where I_w is the light intensity reaching the photoconductor. The expression for I_w is given by [12]

$$I_w = |\mathrm{e}^{\mathrm{i}(L/2k)\nabla_\perp^2}(\sin\psi_1 \sin\psi_2 + \cos\psi_1 \cos\psi_2 \mathrm{e}^{-\mathrm{i}\varphi})|^2 I_{\text{in}}, \tag{2}$$

where $\varphi = \beta\cos^2\theta$ is the overall phase shift experienced by the light travelling forth and back through the liquid crystal layer, θ is the liquid crystal reorientation angle and $\beta = 2kd\,\Delta n$, where $k = 2\pi/\lambda$ is the optical wave number ($\lambda = 633$ nm), $d = 15\,\mu$m is the thickness of the liquid crystal layer and $\Delta n = 0.2$ is the difference between the extraordinary ($\parallel$ to $\vec{n}$) and ordinary ($\perp$ to $\vec{n}$) index of refraction of the liquid crystal.

When $\psi_1 = -\psi_2 = 45$ deg and $L = 0$, that is, in the purely interferential case, Eq. (2) becomes

$$I_w = (1 + \cos\varphi)I_{\text{in}},$$

that gives multi-valued solutions for φ when inserted in Eq. (1). In this case, several branches of bistability between differently oriented states may be observed. In particular, we will focus here on the bistable behaviour shown by the system close to the Fréedericksz transition point.

In the experiment, we set $L = 0$, thus eliminating diffraction, and we adjust the fiber bundle in such a way that there is no rotation or translation in the feedback image. Then, in order to construct the experimental bifurcation diagram, we measure the intensity I_w

reaching the photoconductor. This is done by extracting a small portion of the feedback light and by sending it onto a photodiode. When the applied voltage V_0 is below the threshold for molecular reorientation, I_w has a value fixed by β. When reorientation occurs, we expect this value to change according to expression given in Eq. (2). Variations of I_w induce, on their turn, variations of the effective voltage applied across the liquid crystal film and hence a further reorientation. Once feedback is established between the applied voltage and the liquid crystal director, the Fréedericksz transition becomes subcritical.

A typical bifurcation diagram, as shown in Fig. 2, displays a large hysteresis region. In the bistable region, the nonoriented ($\theta = 0$) and the oriented ($\theta \neq 0$) state coexist. Correspondingly, after the feedback polarizer, we observe a dark ($I_w = 0$) or a white state ($I_w \neq 0$). Note that I_w is measured by a small area photodiode, i.e., it is a local measurement taken at the center of the feedback beam. By looking at the entire image of the beam with a CCD camera, we see that the transition point is characterized by a white spot developing over a dark background. The interface around the white spot is a front, connecting the reoriented region to the nonreoriented one. Three representative images of the feedback field are displayed in Fig. 2, showing the direction of the front propagation in dependence on the mutual stability of the white and the dark states.

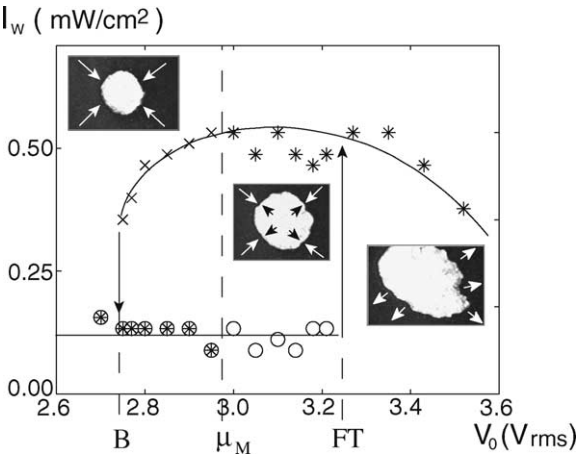

Fig. 2. I_w as a function of the applied voltage V_0: open circles are dark states with writing light off; stars are white states with writing light off; cross are white states with writing light on. The white state shrinks to zero or expands to infinity depending on the initial location of the perturbation. Beyond (and close to) the Maxwell point it exists a critical droplet radius for which the front velocity is zero.

5. Front propagation

In a spatially extended system, a subcritical transition gives rise to a transient behaviour characterized by front dynamics. At the onset of bistability, the system displays moving interfaces, so-called *fronts*, that connect the two stable states. Once created, the front moves into the most energetically favorable state with a well defined velocity. In the case of one or two-dimensional variational system and small interface curvature, the front velocity is proportional to the energy difference between the two states. By increasing the bifurcation parameter, the metastable state becomes energetically equivalent to the other state, thus the front stops propagating. In this case, the system is said to be at the Maxwell point, μ_{M} [39]. By further increase of the bifurcation parameter, the front velocity is reversed, that is, the most energetically favoured state invades the less favoured one.

When the state becomes unstable through a pitchfork bifurcation, there is also a front that connects a stable state with an unstable one. This type of front is called Fisher–Kolmogorov–Petrosvky–Piskunov (FKPP) [40,41]. At variance with the normal front, the velocity of the FKPP front is not determined by the difference of energy between the two connected states. There is instead an infinite set of possible velocities, each one determined by the initial conditions [42,2]. In the case of bounded perturbations of the unstable state, the front propagate with the minimum velocity [42].

In Fig. 2, the dashed line marks the Maxwell point, μ_{M}. Below this point the white state is less stable than the dark one and the white spot, once created by the writing light, contracts to zero. Above the Fréedericksz transition point, FT, the white spot nucleates spontaneously and the front expands until the white state covers all the background. In between, the front expands or retracts depending on the size of the perturbation.

In order to determine the size of the bistable region, we inject an additional light spot (low power He–Ne laser) into the feedback loop. This acts as a small perturbation, triggering the transition from the dark state to

the white one. The white state persists when we block the additional writing light, while it switches to the dark state if we perturb the feedback. In Fig. 2, the arrows delimit the region over which this writing-erasing procedure is robust. The three crucial points, i.e., the beginning of the bistability, B, the Maxwell point, μ_{M}, and the Fréedericksz transition point, FT, are also identified by the divergence of the response times, as it was shown in [26].

In order to measure the front velocity, we have performed quasi-1D experiments, in such a way to minimize the influence of the 2D curvature onto the front velocity. A ring-shaped mask is introduced in the optical setup, in contact to the entrance side of the fiber bundle.

The ring shape of the mask constraints the system to be quasi-1D and to satisfy periodic boundary conditions [27]. The choice of the ring is for the sake of simplicity, but any closed and smooth domain leads to similar results for the front velocity. The inner diameter D of the ring was chosen in between 5 and 10 mm whereas the ring thickness l was between 0.5 and 1 mm, so that the aspect ratio D/l is quite large and the system can be considered as 1D. The large curvature of the ring mask is considered not to affect the front propagation that develops in the transverse direction. Moreover, the ring thickness is considered large enough not to introduce relevant boundary effects.

The velocity of the front propagating between the two differently oriented states has been measured by recording a movie of the front propagation along the ring. Instantaneous snapshots, for $V_0 = 3.05 V_{\mathrm{rms}}$, are shown in Fig. 3. Above the Maxwell point, V_0 is switched on from zero and the front nucleates spontaneously over any inhomogeneities present in the LCLV. To see the front propagation below the Maxwell point, the initial condition for V_0 is chosen in the region of well developed reorientation and then V_0 is switched to a lower value, below Maxwell point. In this case, the front velocity is reversed and the white state contracts to zero. Instantaneous snapshots recorded for $V_0 = 2.84 V_{\mathrm{rms}}$ are shown in Fig. 3

Either below or above the Maxwell point, the front velocity is measured by unfolding the rings over a line

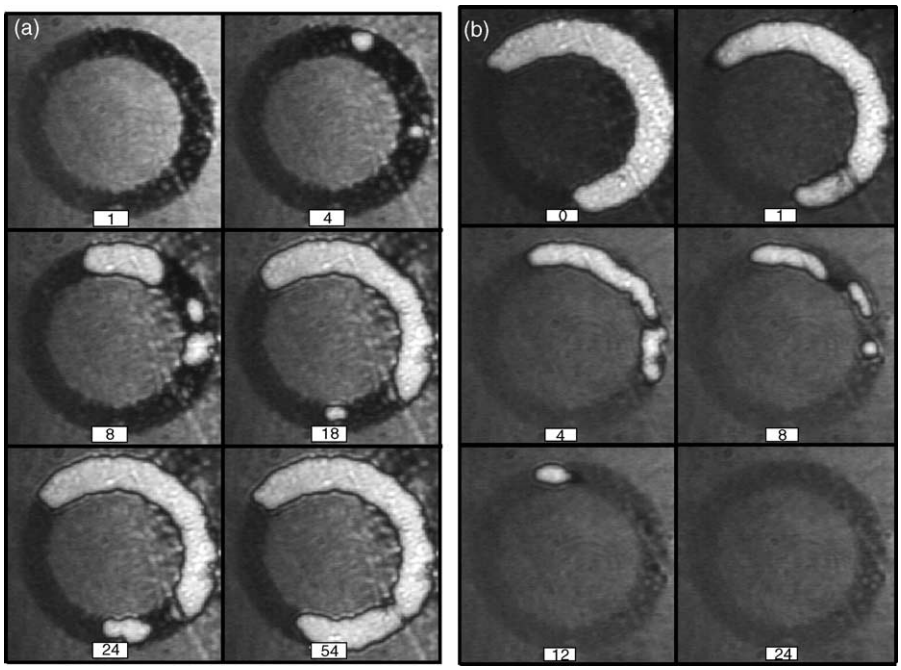

Fig. 3. Snapshots of the front propagation, recorded at (a) $V_0 = 3.05 V_{\mathrm{rms}}$, above the Maxwell point, and (b) $V_0 = 2.84 V_{\mathrm{rms}}$, below the Maxwell point. The successive instant times (in seconds) are indicated in the white labels.

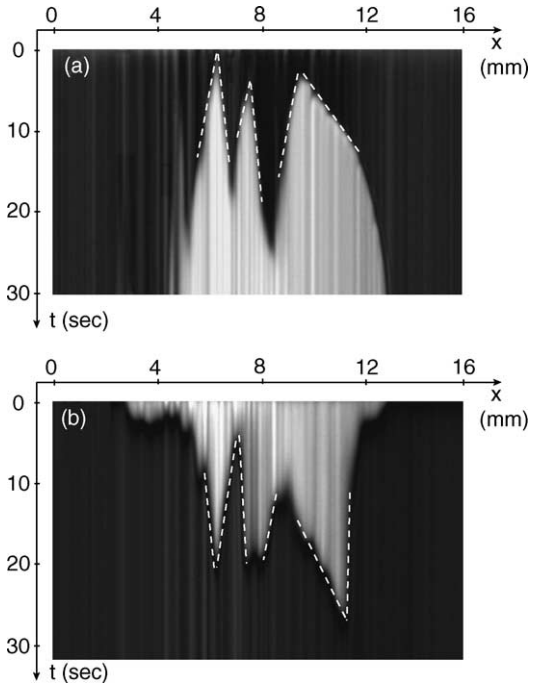

Fig. 4. Spatio-temporal plot showing the propagation of the front at (a) $V_0 = 3.05V_{\rm rms}$, above the Maxwell point, and (b) $V_0 = 2.84V_{\rm rms}$, below the Maxwell point. Dashed lines mark the slope of the regions used to evaluate the front velocity.

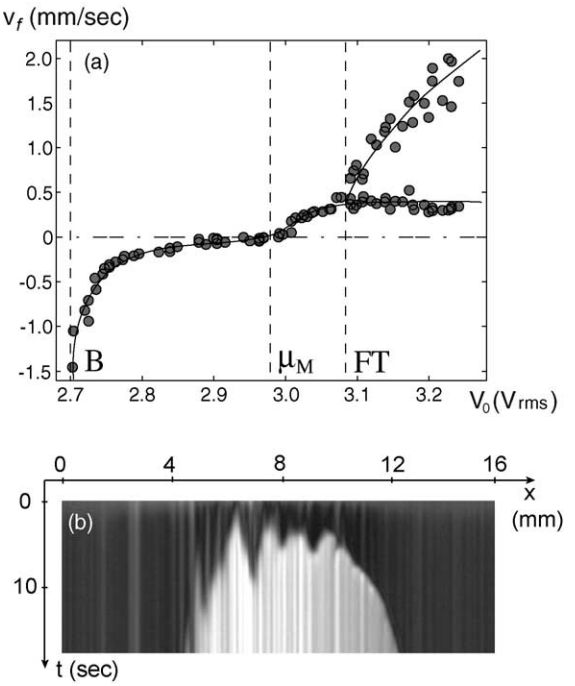

Fig. 5. (a) Front velocity as a function of the bifurcation parameter V_0. Solid lines are guides for the eyes. Dashed lines mark the three critical points: B, $\mu_{\rm M}$, FT. (b) Spatio-temporal plot showing the propagation of a FKPP front ($V_0 = 3.2V_{\rm rms}$).

and by constructing the corresponding spatio-temporal diagrams, as shown in Fig. 4. The front velocity can be evaluated by measuring the ratio between the horizontal (space – x) and vertical (time – t) displacements. Note that LCLV inhomogeneities introduce a pinning of the front in particular spatial locations, so that the front stops or largely slow down at these places. When measuring the front velocity, we have averaged only the slopes of the linear portions on the spatio-temporal plots, such as the ones marked by the dashed lines in Fig. 4. Pinning of the front over LCLV inhomogeneities is also responsible for the stripe patterning which appears on the spatio-temporal plots.

The resulting front velocities are plotted in Fig. 5 as a function of the applied voltage V_0. On this figure, we can identify the Maxwell point, where the front velocity goes to zero, and the FT point, beyond which the fronts become of a FKPP type. The regime of FKPP fronts is characterized by a transient propagation with a quite high velocity, which then relaxes to the minimal one. In Fig. 5the transient and the steady-state velocities correspond to the upper and lower branch, respectively. In the inset of Fig. 5it is shown a spatio-temporal diagram for a FKPP front, where it is possible to distinguish the nonlinear transient characterizing the early times of the front propagation.

6. The amplitude equation near the Fréedericksz transition point

Near the Fréedericksz transition point we can develop a theoretical model starting from the physics of the nematic liquid crystals. The Fréedericksz transition takes place when the electric torque overcomes the elastic restoring force. The competition between the elastic and the electric forces is ruled by the Frank free energy [32]. In the LCLV, as a consequence of the optical feedback, the electric field $\vec{E}$, that locally apply to the liquid crystals, depends on the director $\vec{n}$. Thus, the variation δF of the free energy, resulting from a variation $\delta\vec{n}$ of

the director, takes the form

$$\delta F = \frac{1}{2}\int \delta[K_1(\vec{\nabla}\cdot\vec{n})^2 + K_2(\vec{n}\cdot(\vec{\nabla}\wedge\vec{n}))^2]d^3x + \frac{1}{2}\int \delta[K_3(\vec{n}\wedge(\vec{\nabla}\wedge\vec{n}))^2]d^3x - \int \vec{E}\delta\vec{D}(\vec{n})d^3x, \quad (3)$$

where K_1, K_2 and K_3 are the elastic constants describing the elastic deformation of the nematic film for splay, twist and bend, respectively, and the last integral accounts for the electromagnetic contribution. The displacement vector $\vec{D}$ is related to the director by $\vec{D} = (\epsilon_\perp/2)\vec{E}(\vec{n}) + (\epsilon_a/2)(\vec{n}\cdot\vec{E}(\vec{n}))\vec{n}$, with ϵ_a being the dielectric anisotropy and $\epsilon_\perp$ the perpendicular dielectric permeability.

The variation of the displacement vector is

$$\delta\vec{D} = \frac{\epsilon_\perp}{2}\frac{\partial\vec{E}(\vec{n})}{\partial\vec{n}}\delta\vec{n} + \frac{\epsilon_a}{2}(\delta\vec{n}\cdot\vec{E}(\vec{n}))\vec{n} + \frac{\epsilon_a}{2}(\vec{n}\cdot\vec{E}(\vec{n}))\delta\vec{n} + \frac{\epsilon_a}{2}\left(\vec{n}\frac{\partial\vec{E}(\vec{n})}{\partial\vec{n}}\delta\vec{n}\right)\vec{n},$$

where $\partial\vec{E}/\partial\vec{n}$ is a tensor of order two with $(\partial\vec{E}/\partial\vec{n})_{i,j} = \partial E_i/\partial n_j$. The dynamical equation for the liquid crystal director is given by

$$\gamma\vec{n}\wedge\partial_t\vec{n} = -\vec{n}\wedge\frac{\delta F}{\delta\vec{n}}, \quad \vec{n}\vec{n} = 1,$$

where γ is the rotational viscosity of the nematic film.

For the sake of simplicity, we assume $K_1 = K_2 = K_3 = K$. Thus, the dynamical equation reads

$$\gamma\partial_t\vec{n} = K[\nabla^2\vec{n} - \vec{n}(\vec{n}\cdot\nabla^2\vec{n})] + \epsilon_a(\vec{n}\cdot\vec{E})[\vec{E} - \vec{n}(\vec{n}\cdot\vec{E})] + \frac{\epsilon_\perp}{4}\frac{\partial\vec{E}^2}{\partial\vec{n}} - \frac{\epsilon_\perp}{4}\left[\vec{n}\cdot\frac{\partial\vec{E}^2}{\partial\vec{n}}\right]\vec{n} + \frac{\epsilon_a}{2}\times(\vec{n}\cdot\vec{E})\left[\frac{\partial\vec{E}}{\partial\vec{n}}\cdot\vec{n} - \left(\vec{n}\cdot\left(\frac{\partial\vec{E}}{\partial\vec{n}}\cdot\vec{n}\right)\right)\vec{n}\right],$$

where $\partial\vec{E}/\partial\vec{n}\cdot\vec{n} = n_x\vec{\nabla}E_x + n_y\vec{\nabla}E_y + n_z\vec{\nabla}E_z$.

At rest (without any electric field applied), the liquid crystal alignment is planar, that is, all the molecules are parallel to the x-axis (x and y being in the plane of the confining plate and z perpendicular to it), so that $\vec{n} = (1, 0, 0)$. In the presence of an electric field applied along z, $\vec{E} = (0, 0, E_z)$ and for $\epsilon_a > 0$, the director reorients in the x–z plane. As a consequence, the director becomes $\vec{n} = (n_x, 0, n_z)$ with $n_x^2 + n_z^2 = 1$.

In the absence of light on the photoconductor, the electric field E_z applied to the liquid crystal layer is $E_{z(I_w=0)} \equiv E_{(I_w=0)} = \Gamma E_0 = \Gamma V_0/d$, where V_0 is the total voltage applied to the LCLV, and $\Gamma < 1$ is a transfer factor that depends on the electrical characteristics of the photoconductor, dielectric mirror and liquid crystal layers (impedances). As long as the light intensity is sufficiently small, that is, of the order of a few mW/cm^2, the response of the photoconductor can be fitted by a linear function. Under this approximation, the total effective electric field applied to the liquid crystal film can be expressed as $E_{\text{eff}} = E_{(I_w=0)} + \alpha I_w$, where α is a phenomenological dimensional parameter that can be evaluated from the characteristics of the LCLV [27].

After substituting the write intensity I_w, Eq. (2), in the expression for the electric field, we obtain

$$E(\vec{n}) = E_{(I_w=0)} + \alpha I_w(\vec{n}) = E_{(I_w=0)} + \alpha I_{\text{in}}[A + B\cos(\beta\cos^2\theta)], \quad (4)$$

where

$$A = \tfrac{1}{4}[\cos 2(\psi_1 - \psi_2) + \cos 2(\psi_1 + \psi_2) + 2],$$
$$B = \tfrac{1}{4}[\cos 2(\psi_1 - \psi_2) - \cos 2(\psi_1 + \psi_2)], \quad (5)$$

where ψ_1 and ψ_2 are, respectively, the angles formed by the input and feedback polarizers with the nematic director $\vec{n}$.

Close to the onset of the Fréedericksz transition, the director reorientation can be expressed as a Fourier series $n_z(x, y, z, t) = \sum_n u_n(x, y, t)\sin(n\pi z/d)$. For a small reorientation angle, the director reorientation along the z direction, n_z, describes quite well the orientation angle of the liquid crystal molecules. By means of the standard bifurcation theory [2], it is possible to derive an amplitude equation for the first unstable Fourier mode, $n_z = u(x, y)\sin(\pi z/d)$ and $n_x = 1 - u^2\sin^2(\pi z/d)/2$. The amplitude equation reads

$$\partial_t u = c_1 u + c_3 u^3 + c_5 u^5 + \frac{K}{\gamma}\nabla_\perp^2 u, \quad (6)$$

where the development has been extended up to the fifth order since the third order coefficient c_3 can become positive depending on the parameters of the system.

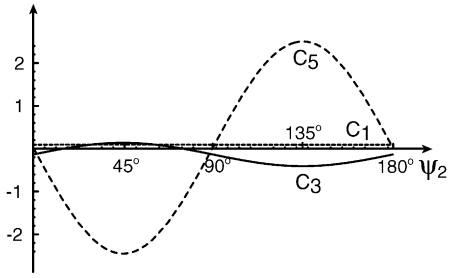

Fig. 6. Coefficients c_1 (dotted line), c_3 (continuous line) and c_5 (dashed line) as a function of the polarizer angle ψ_2 (radian). The system is close at the onset of the bifurcation, that is, c_1 is close to zero, and $\psi_1 = -45$ deg.

The amplitude equation, Eq. (6), describes qualitatively the subcritical bifurcation close to the Fréedericksz transition point. The coefficients c_1, c_3 and c_5 are functions of the physical parameters of the experiments, that is, c_1, c_3 and c_5 are functions of $\beta, \epsilon_\perp$, ϵ_a, E_0, I_{in}, ψ_1, ψ_2. The three coefficients may change sign depending on the parameters set in the experiment, and in particular the sign of c_3 depends on the polarization angles ψ_1 and ψ_2 [26,27]. Note that A and B are periodic in ψ_1 and ψ_2, so that changing the polarizer angles modulates the response of the LCLV. When c_3 is negative and of order one, Eq. (6) describes a second order Fréedericksz transition. This transition becomes of a first-order one when c_1 and c_3 are positive (and small) with c_5 negative. The complete expression of the coefficients is reported in [27].

In Fig. 6 c_3 and c_5 are reported as a function of ψ_2 and for a fixed value of $\psi_1 = -45$ deg. The first coefficient c_1 is set close to zero in order to keep the system close to the transition point. The other parameters are fixed at the experimental values. As we can see on the plot, c_3 becomes positive for small values of ψ_2, whereas c_5 is already negative, thus assuring the saturation of the amplitude. In particular, the values set in the experiment, $\psi_2 = -\psi_1 = 45$ deg, assure that the Fréedericksz transition becomes of first-order.

In Fig. 7a it is shown a phase diagram in the plane of the input light intensity I_{in} and of the polarizer angle ψ_2. The applied electric field E_0 is computed in order to set the system at the bifurcation point, that is, at $c_1 = 0$. Then, we look at the sign of c_3 to determine whether the bifurcation is subcritical or supercritical. The line marks the transition between the two cases, corresponding to $c_3 = 0$. The phase diagram characterizes entirely the dependence of c_3 from the physical parameters that are readily accessible from the experimental side. Changing the value of c_3 leads to tuning the character of the Fréedericksz transition, from a largely subcritical one to a small subcriticality or even to supercriticality.

It is important to remark that in the general case of nascent bistability the bifurcation is associated to a cusp catastrophe in the space of parameters. However, this picture can change when the system presents a symmetry, like the reflection symmetry, as it occurs for the Fréedericksz transition. In this case, the system goes

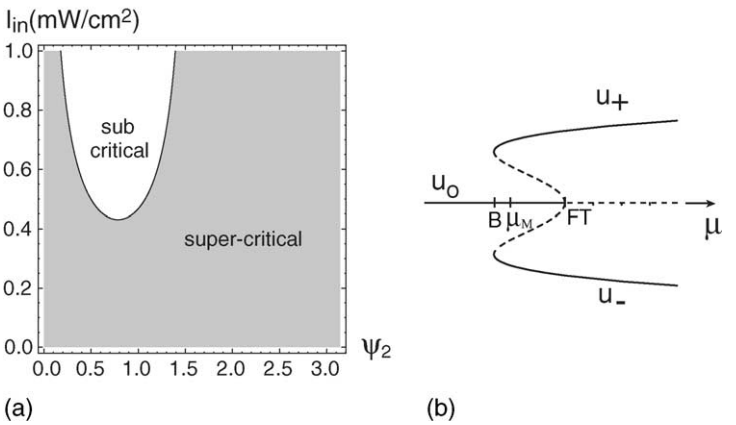

Fig. 7. (a) Phase diagram as a function of the input intensity I_{in} and of the polarizer angle ψ_2 (radian). Solid line corresponds to $c_3 = 0$, marking the border between the subcritical and the supercritical case. (b) Bifurcation diagram in the subcritical case (μ is the bifurcation parameter).

through a pitchfork bifurcation and the reoriented state u is equivalent to the $-u$ state, as it is schematically depicted in Fig. 7b. Correspondingly, in the parameter space, the catastrophe becomes smooth, like it is shown in Fig. 7a, at variance with the cusp singularity. At the transition line between the sub and supercritical regimes the bifurcation diagram looks like a pitchfork bifurcation, but the equilibrium state as a function of the bifurcation parameter scales as $\mu^{1/4}$, at variance with the supercritical bifurcation where it scales as $\mu^{1/2}$.

7. Localized structures and crystal-like symmetries

When we insert a free propagation length L in the feedback loop, the system displays localized structures. Fig. 8 displays typical distributions of localized structures, observed for $L = -10\,\mathrm{cm}$, an applied voltage $V_0 = 18.45 V_{\mathrm{rms}}$ at 5 kHz frequency and a feedback rotation angle $\Delta = 2\pi/N$ with $N = 6$. The size of each individual spot is approximately $\Lambda = 350\,\mu\mathrm{m}$, which corresponds to the basic wavelength $\Lambda = 2\pi/q_0 = \sqrt{2\lambda L}$ ($\lambda = 633\,\mathrm{nm}$ is the optical wavelength) predicted by the linear analysis for a focusing medium with a feedback mirror [36]. The distance between the spots is in average much larger than their size, which indicates that we deal with a collection of localized structures instead of a fully correlated pattern.

Here, for a fully correlated pattern we mean an extended spatial structure that cannot, in any case, be decomposed into its basic cells. For example, in a full pattern of hexagons, like the ones arising in thermal convection [2], we cannot destroy a single cell without destroying the whole pattern or without avoiding that the cell be replaced by another one. In the case of localized structures, even though an overall correlation may be imposed by the geometrical constraints, each cell of the pattern is independent of the whole configuration and may be addressed as a single element [43]. In our case, for the symmetry imposed by the rotation angle, the basic independent element that we have to consider is a set of N structures, always appearing along concentric rings. The center is a singular point, that may or not be occupied by a localized structure, depending on the initial condition. The recurrence constraint imposed by the feedback rotation stabilizes the positions of the localized structures that, once created, remains fixed to their positions.

The input light intensity is fixed to $I_{\mathrm{in}} = 0.9\,\mathrm{mW/cm^2}$, a value close to the point of nascent bistability. Different stationary configurations may be obtained, depending on the initial condition. The resulting configurations stay stable for several minutes. If we perturb the system by blocking the feedback loop, another configuration may appear. Actually, close to the point of nascent bistability, the dark homogeneous state is also stable. Thus, once erased by blocking the

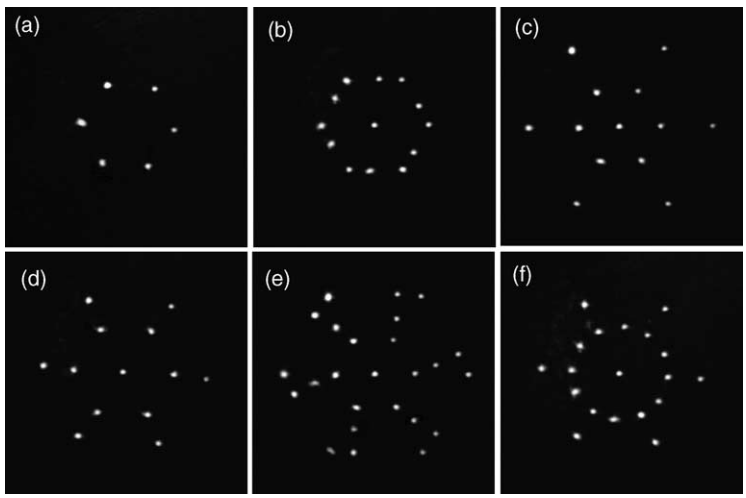

Fig. 8. Near-field images of localized structure configurations recorded for $\Delta = 2\pi/N$ with $N = 6$ and for different initial conditions.

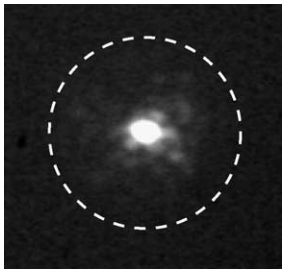

Fig. 9. A typical image observed in the far-field when the near-field displays localized structures.

feedback loop, there are no localized structures until we introduce a perturbation able to trigger their appearance. This can be done either by slightly, and temporarily, increasing V_0, or by injecting in the feedback loop a weak additional light beam, such as the one of a commercial laser pointer. With the laser pointer, it is possible to address different positions for the excitation of localized structures. Starting from a single set of N localized structures, we can locally perturb the system and switch on another set in a different position or a single spot in the center. All these manipulations prove that the observed spots are indeed localized structures, in the sense that the whole pattern is highly decomposable, that is, each structure may be considered as a single element, independent of the other structures [43].

The localization in the near-field manifests his counterpart as a strong delocalization in the far-field. Indeed, observations in the far-field show a diffusion of the light intensity around the central peak (zero spatial frequency). In the same time, no wave vector structure is distinguishable. A typical far-field image is displayed in Fig. 9, where the dashed line marks the location that would be occupied by the wave vectors of a fully correlated pattern, at the spatial frequency $q_0 = 2\pi/\Lambda$, corresponding to the size of the individual spots. The same diffraction pattern is observed in the far-field also by changing the symmetry of the near-field distributions, as we have verified for several cases by changing Δ.

Another related aspect of the localization is that the near-field patterns assume the aspect of what it is normally expected to appear in the far-field. By choosing $\Delta = 2\pi/N$ with different N we can construct in the real space a highly regular distribution of light spots, that can be seen as the structure function (in the Fourier space) of a corresponding N-order crystal. By keeping

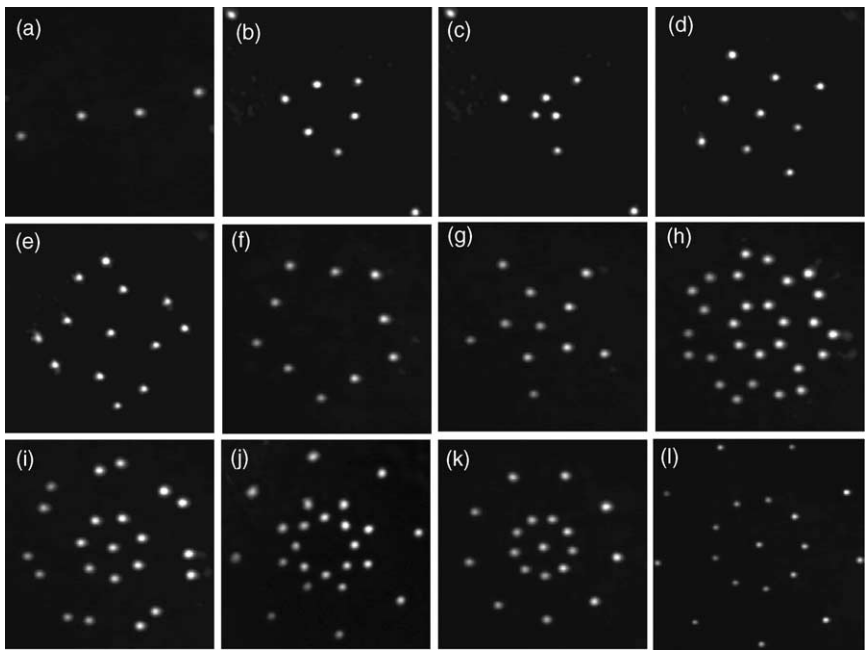

Fig. 10. Near-field images of stationary localized structures observed for $\Delta = 2\pi N$ with (a) $N = 2$, (b, c) $N = 3$, (d, e) $N = 4$, (f, g) $N = 5$, (h, i) $N = 7$, (j) $N = 8$ and (k, l) $N = 9$. In (l) the magnification factor is 2/3 with respect to the other frames.

the input light intensity close to the point of nascent bistability, the spots remain fixed to their position and we can control their appearance and position by means of a local writing procedure. This is very appealing for the possibility to synthesize in the real space a sort of "crystallography", where all the N rotational-order structures may be figured out.

A few examples are displayed in Fig. 10, where we show the crystal and quasi-crystal like distributions of light spots that are observed for $\Delta = 2\pi N$ with $N = 2, 3, 4, 5, 7, 8, 9$. Note that these N-order spot distributions, here observed for a complete localization in the near-field, are the spectral counterpart of the spatially extended crystals and quasi-crystals that appear in the near-field of a LCLV experiment, when a perfect localization is instead manifested in the far-field [44].

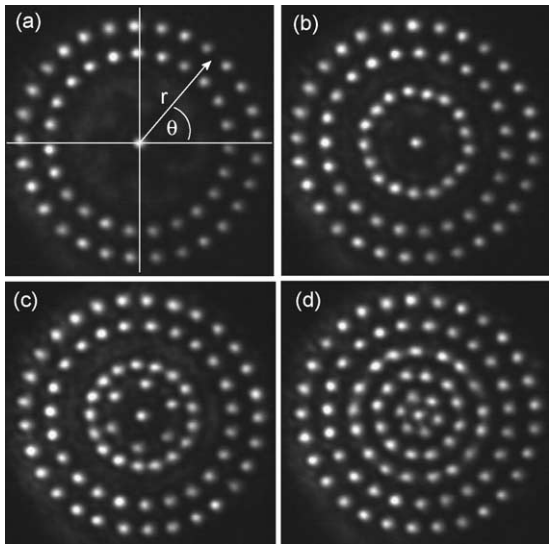

Fig. 11. Instantaneous snapshots of localized structures for $\Delta = 2\pi/N + \delta$ with $N = 6$ and $\delta = 0.1$ deg. The number of rings is increasing during time: (a) $t = 0$, (b) $t = 5$, (c) $t = 10$ and (d) $t = 22$ s.

8. Dynamics of localized structures

8.1. Ring dynamics induced by a nonlocal shift in the feedback loop

If we introduce a small additional rotation angle, $\delta = 0.1$ deg, in such a way that $\Delta = 2\pi/N + \delta$, the localized structures acquire a rotation dynamics along concentric rings. Even though the nonlocal shift, δ, is along one direction, often, two adjacent rings rotate in opposite directions.

For $\Delta = 2\pi/N + \delta$, with $N = 6$ and $\delta = 0.1$ deg, we have set the applied voltage to $V_0 = 18.49 V_{\rm rms}$ (5 kHz) and we have studied the dynamics of localized structures. For this value of V_0, the structures appear spontaneously, nucleating from the intrinsic noise in the LCLV (inhomogeneities or fluctuations). Moreover, in the vicinity of the bistability point, the slight gradients provided by the Gaussian beam profile are imposing the O(2) circular symmetry, leading to the appearance of successive and concentric rings. We expect that other shapes of the beam profile or different initial conditions would lead to different distributions of localized structures, as shown numerically in [38]. Note that similar near-field patterns, *Akhseals*, have also been reported by the Akhmanov group [24]. Even though not explained in terms of localized structures, they are indeed observed in experimental conditions similar to ours.

After their creation, the structures are characterized by a complex spatio-temporal dynamics, developing both along the radial and the azimuthal directions. The spots rotates over the rings and the ring diameter also changes during the time. Eventually, the radial motion may lead to the collapse of two adjacent rings or to the splitting of one ring into two neighboring ones. Near-field snapshots showing this dynamical behaviour are displayed in Fig. 11. It can be noticed that each ring reflects the underlying hexagonal symmetry, so that the number of spots is 6 on the inner ring and increases by step of 6 over two adjacent ones. However, for the outer rings, the number of spots is 17, 23, 29, that is, one spot is missing with respect to the underlying $N = 6$ hexagonal symmetry. In a similar way, for other values of N we find either an exceeding or a missing spot on the outer rings [16].

In Fig. 12 azimuthal ($\theta - t$), spatio-temporal plots are reported as an example of the rings dynamics. Fig. 12a and b show, respectively, the rotation of the localized structures over the 12 and 17 spot rings. Note that the two rings are counter-rotating with different speed of rotation. At longer times, eventually each ring undergoes a radial instability, leading to creation and annihilation of adjacent rings. An example is shown in

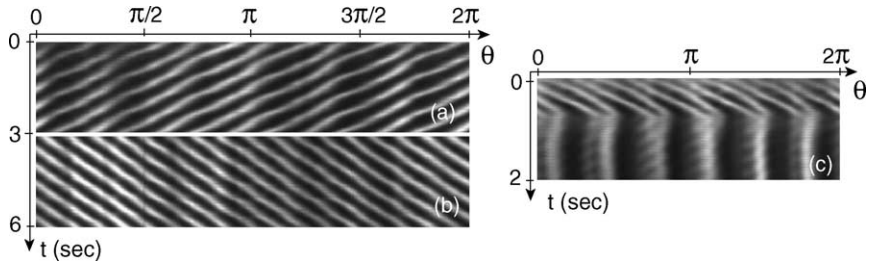

Fig. 12. Azimuthal ($\theta - t$) space-time plots for (a) 12-spots and (b) 17-spots ring; (c) shows the transition from 12 to 6 spots.

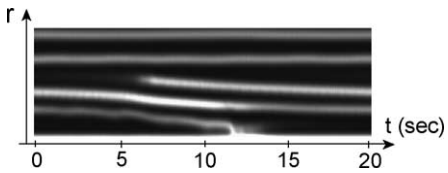

Fig. 13. Radial ($r - t$) space-time plot showing the creation and annihilation of rings.

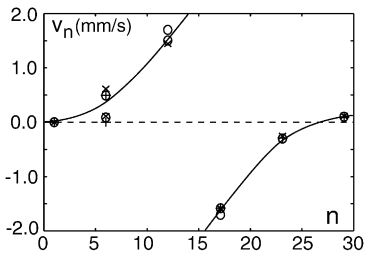

Fig. 14. Speed of rotation for increasing number n of localized structures along the successive rings.

Fig. 12c where, the fusion of two adjacent spots leads to the transition from 12 to 6 localized structures. In the azimuthal plots the radial distance is normalized to the instantaneous diameter of each ring. In Fig. 13 is shown a radial ($r - t$), spatio-temporal plot (averaged over θ), where the ring creation-annihilation may be distinguished.

We show in Fig. 14 the measured speed of rotation v_n for increasing number n of spots along the successive rings. It must be recalled that the diameter of the rings is not constant during time, so that the number n is only roughly related to the distance from center. The measured data suggest that the change of rotation direction could be related to the existence of a critical radius, above which an overall phase shift changes its sign. Correspondingly, the number of spots along the outer rings becomes "wrong".

8.2. Intrinsic dynamics of localized structures

As a consequence of the nonvariational character of the LCLV experiment, we expect the localized structures to exhibit an intrinsic and permanent dynamics for some range of the control parameters. Indeed, as we slightly increase the input light intensity above the point of nascent bistability, we observe oscillations in the positions of the localized structures, and this even though the feedback rotation angle Δ is exactly fixed to a value commensurate to 2π. In Fig. 15 we show the instantaneous snapshots of the $N = 5$ distributions observed in the same experimental conditions as for Fig. 10f–g and by increasing the input light intensity to $I_{\text{in}} = 0.95\,\text{mW/cm}^2$. The observed dynamics consist of a periodic bouncing of two adjacent spots one over the other.

The periodic behaviour can be extracted by plotting a spatio-temporal plot along a line passing through the centers of two adjacent spots, as shown by the dashed line in Fig. 15a. The resulting diagram is displayed in Fig. 15e. By further increase of I_{in} the oscillations in the structure positions become irregular in time. Similar dynamical behaviours can be observed for all the other N-order distributions of localized structures.

In order to single out the dynamics independently of the symmetry imposed by the feedback rotation angle Δ, we have carried out one-dimensional experiments by fixing $\Delta = 0\,\text{deg}$. In this case, the system becomes very sensitive to the influence of optical misalignments, such as small drifts, inhomogeneities or any other source of small gradients. We have selected the one-dimensional region on a central part of the LCLV, where illumination gradients and misalignment effects are negligible. A rectangular mask is introduced

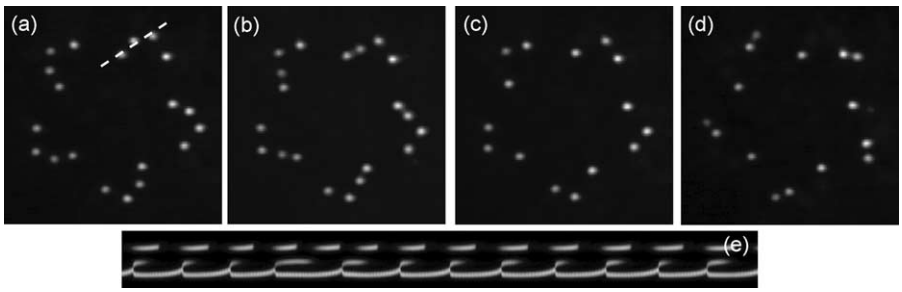

Fig. 15. Instantaneous snapshots showing the oscillations of the localized structure positions. Times: (a) 0.0, (b) 2.6, (c) 5.0, (d) 8.2 s. The dashed line in (a) marks the one-dimensional cut along which the spatio-temporal diagram has been recorded. (e) Space (vertical)-time (horizontal) diagram showing the periodic oscillations of the structure positions. The total elapsed time is 120 s.

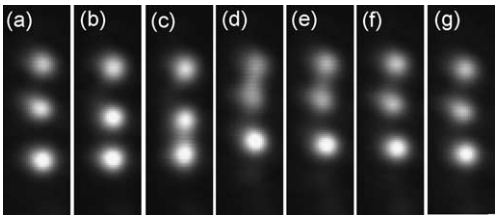

Fig. 16. Instantaneous snapshots showing three bouncing localized structures. Times: (a) 0.0, (b) 1.0, (c) 1.3, (d) 1.7, (e) 2.1, (f) 2.4 and (g) 2.8 s.

in the optical feedback loop, just in contact to the entrance side of the fiber bundle. The width D of the aperture is 0.50 mm whereas its length l is 20 mm. The transverse aspect ratio $D/\Lambda \simeq 1$ is small enough for the system to be considered as one-dimensional, whereas the longitudinal aspect ratio $l/\Lambda \simeq 60$ is large enough for the system to be considered as a spatially extended one. In Fig. 16 are shown the instantaneous snapshots of three adjacent localized structures, with two of them bouncing periodically in time one over the other. The corresponding spatial profiles are plotted in Fig. 17 whereas in Fig. 18b it is displayed the corresponding spatio-temporal plot. Besides, Fig. 18a represents two stationary localized structures, whose position remains fixed during time and Fig. 18c is the spatio-temporal diagram corresponding to the aperiodic oscillations in the positions of two adjacent localized structure.

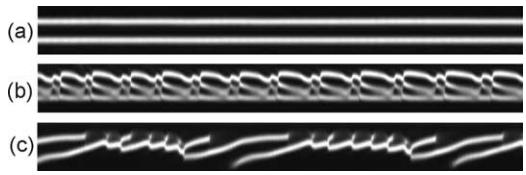

Fig. 18. Space (vertical)-time (horizontal) diagrams showing (a) two stationary localized structures, (b) the periodic and (c) the aperiodic oscillations of the structure positions. The total elapsed time is 94 s.

9. The model beyond the Fréedericksz transition

When we move beyond the Fréedericksz transition, a one-dimensional model can be setup starting from the standard description of the optical feedback loop [12]. By taking into account both diffraction and polarization interference, the light intensity I_w reaching the photoconductor is given by

$$I_w = \tfrac{1}{2} I_{\rm in} |{\rm e}^{{\rm i}(L/2k)\partial_{xx}}(1 + {\rm e}^{-{\rm i}\beta\,\cos^2\theta})|^2$$

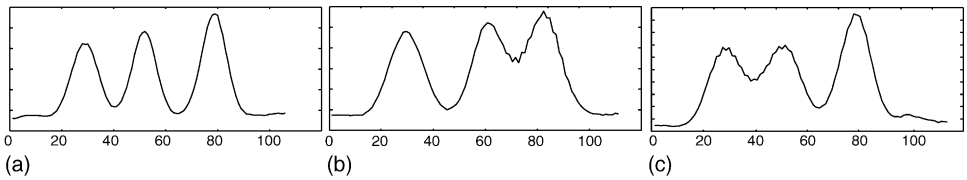

Fig. 17. Spatial profile of the localized structures. Times: (a) 0.0, (b) 1.3 and (c) 1.7 s. The horizontal scale is in pixel units.

where x is the transverse direction of the liquid crystal layer.

Let us introduce the average director tilt, $\theta = \theta(x, t)$, of the director. $\theta = 0$ is the initial unperturbed planar alignment whereas $\theta = \pi/2$ is the homeotropic alignment corresponding to the saturation of the molecular reorientation. The liquid crystal dynamics is described by a local relaxation equation of the form

$$\tau\partial_t\theta = l^2\partial_{xx}\theta - \theta + \frac{\pi}{2}\left(1 - \sqrt{\frac{V_{FT}}{\Gamma V_0 + \alpha I_w(\theta, \partial_x)}}\right) \tag{7}$$

with $V \equiv \Gamma V_0 + \alpha I_w(\theta, \partial_x) > V_{\mathrm{FT}}$, where V_{FT} is the Fréedericksz transition threshold voltage and l is the electric coherence length. The above model have been deduced by fitting the experimental data measured for the open loop response of the LCLV [27,25] and it is slightly different with respect to the one proposed in Ref. [12].

The homogeneous equilibrium solutions are $\theta_0 = \pi/2(1 - \sqrt{V_{\mathrm{FT}}/V})$ when $V > V_{\mathrm{FT}}$ and $\theta_0 = 0$ when $V \leq V_{\mathrm{FT}}$. The graph of $\theta_0(V_0, I_{\mathrm{in}})$ is shown in Fig. 19 for a value of I_{in} close to the experimental conditions. Several successive branches of bistability can be distinguished, corresponding to the critical points where $\theta_0(V_0, I_{\mathrm{in}})$ is a multi-valued function. Note that once the reorientation takes place, that is, $\theta_0 \neq 0$, the system loose the inversion symmetry around the equilibrium solutions. Moreover, the spatial dependence of I_w is nonlocal, hence the dynamics of the above model, Eq. (7), is of nonvariational type, that is, the system cannot be described by a Lyapunov functional.

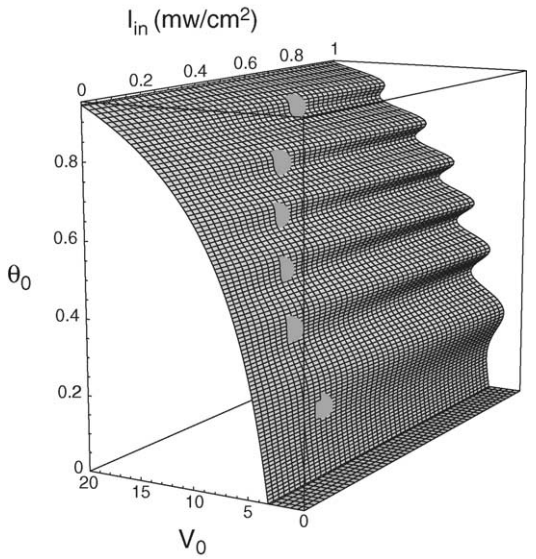

Fig. 19. The multi-valued function $\theta_0(V_0, I_w)$.

Close to each point of nascent bistability (in Fig. 19 the points of nascent bistability are represented by the bright circles), and neglecting the spatial derivatives, we can develop $\theta = \theta_0 + u + \cdots$ and derive a normal form equation

$$\partial_t u = \eta + \mu u - u^3 + \text{h.o.t.}, \tag{8}$$

where μ is the bifurcation parameter and η accounts for the asymmetry between the two homogeneous states. The higher order terms are ruled out by the scaling analysis, since $u \sim \mu^{1/2}$, $\eta \sim \mu^{3/2}$ and $\partial_t \sim \mu$, $\mu \ll 1$. If we now consider the spatial effects, due to the elasticity of the liquid crystal and to the light diffraction, the system exhibits a spatial instability as a function of the diffraction length. The confluence of the nascent bistability and the spatial bifurcation give rise to a multicritical point of codimension three. Close to this point, we derive an amplitude equation, that we call the Lifshitz normal form [28]

$$\partial_t u = \eta + \mu u - u^3 + \nu\partial_{xx}u - \partial_{xxxx}u + du\partial_{xx}u + c(\partial_x u)^2, \tag{9}$$

where $\partial_x \sim \mu^{1/4}$, $\nu \sim \mu^{1/2}$ accounts for the intrinsic length of the system, $d \sim \mathrm{O}(1)$ and $c \sim \mathrm{O}(1)$. The term $\partial_{xxxx}u$ is a kind of super-diffusion, accounting for the short distance repulsive interaction, whereas the terms proportional to d and c are, respectively, the nonlinear diffusion and convection. The full and lengthy expressions of the coefficients for the LCLV will be reported elsewhere [45].

The model shows bistability between a homogeneous and a spatially periodic solutions and therefore it exhibits a family of localized structures. Depending on the choice of the parameters, the localized structures may show periodic or aperiodic oscillations of their position. Numerical simulations of Eq. (9) show a qualitative agreement with the experimental observations [25]. Moreover, there is a quantitative agreement between the location of the points of nascent bistability predicted by the surface of equilibrium states and those observed in the experiment.

10. Conclusions

In the LCLV experiment, we have singled out a regime of parameters where the response of the LCLV is closely similar to that of a binary phase slice working around a point of nascent bistability. In these conditions, and by changing the feedback rotation angle $\Delta = 2\pi/N$, we are able to control the appearance of N-ordered configurations of localized structures, that can be seen as the spectral components of a crystal or a quasi-crystal structure functions. By introducing a small nonlocal shift in the feedback loop, localized structures display a dynamical motion over concentric rings.

Moreover, localized structures are characterized by an intrinsic dynamics. Indeed, when the input light intensity is slightly increased above the point of nascent bistability, the localized states show complex behaviours like the periodic or aperiodic oscillations of their positions. We have related the intrinsic dynamics of the localized structures to the nonvariational character of the system under study and we have derived a generic model taking it into account. The model is a Lifshitz normal form equation, that could be in general applied to a large class of different physical systems, the main requirements being the bistability and the presence of an intrinsic spatial length.

Acknowledgments

We gratefully acknowledge René Rojas for his help in calculations. M.G. Clerc thanks the support of FONDECYT project 1020782, and FONDAP grant 11980002.

References

[1] G. Nicolis, I. Prigogine, Self-organization in Non Equilibrium Systems, Wiley, New York, 1977.
[2] For a review on pattern formation see e.g. M. Cross, P. Hohenberg, Rev. Modern Phys. 65 (1993) 581.
[3] S. Fauve, O. Thoual, Phys. Rev. Lett. 64 (1990) 282.
[4] H.A. Eschenfelder, Magnetic Bubble Technology, Springer-Verlag, Berlin, 1981.
[5] S. Pirkl, P. Ribiere, P. Oswald, Liq. Cryst. 13 (1993) 413.
[6] A. Astrov, Y.A. Logvin, Phys. Rev. Lett. 79 (1997) 2983.
[7] K.-J. Lee, W.D. McCormick, J.E. Pearson, H.-L. Swinney, Nature 369 (1994) 215.
[8] P.B. Umbanhowar, F. Melo, H.L. Swinney, Nature 382 (1996) 793.
[9] O. Lioubashevski, H. Arbell, J. Fineberg, Phys. Rev. Lett. 76 (1996) 3959;
O. Lioubashevski, Y. Hamiel, A. Agnon, Z. Reches, J. Fineberg, Phys. Rev. Lett. 83 (1999) 3959.
[10] K. Lerman, E. Bodenschatz, D.S. Cannell, G. Ahlers, Phys. Rev. Lett. 70 (1993) 3572.
[11] D.W. McLaughlin, J.V. Moloney, A.C. Newell, Phys. Rev. Lett. 51 (1983) 75.
[12] R. Neubecker, G.L. Oppo, B. Thuering, T. Tschudi, Phys. Rev. A 52 (1995) 791.
[13] P.L. Ramazza, S. Ducci, S. Boccaletti, F.T. Arecchi, J. Opt. B 2 (2000) 399.
[14] Y. Iino, P. Davis, J. Appl. Phys. 87 (2000) 8251.
[15] P.L. Ramazza, E. Benkler, U. Bortolozzo, S. Boccaletti, S. Ducci, F.T. Arecchi, Phys. Rev. E 65 (2002) 066204-1.
[16] S. Residori, T. Nagaya, A. Petrossian, Europhys. Lett. 63 (2003) 531.
[17] B. Schäepers, M. Feldmann, T. Ackemann, W. Lange, Phys. Rev. Lett. 85 (2000) 748.
[18] S. Barland, et al., Nature 419 (2002) 699.
[19] P. Coullet, Int. J. Bifurcat. Chaos (2002) and references therein.
[20] G.S. McDonald, W.J. Firth, J. Opt. Soc. Am. B 10 (1993) 1081.
[21] M. Tlidi, P. Mandel, R. Lefever, Phys. Rev. Lett. 73 (1994) 640.
[22] M. Brambilla, L.A. Lugiato, M. Stefani, Europhys. Lett. 34 (1996) 109.
[23] W. Firth, A.J. Scroggie, Phys. Rev. Lett. 76 (1996) 1623.
[24] S.A. Akhmanov, M.A. Vorontsov, V.Yu. Ivanov, JETP Lett. 47 (1988) 707;
M.A. Vorontsov, W.B. Miller, Self-organization in Optical Systems and Applications in Information Technology, Springer, Berlin, 1995.
[25] M.G. Clerc, A. Petrossian, S. Residori, Phys. Rev. Lett., submitted for publication.
[26] M.G. Clerc, S. Residori, C.S. Riera, Phys. Rev. E 63 (2001) 060701(R).
[27] M.G. Clerc, T. Nagaya, A. Petrossian, S. Residori, C.S. Riera, Eur. Phys. J. D 28 (2004) 435.
[28] M.G. Clerc, Phys. Lett. A, submitted for publication.
[29] Y. Kuramoto, Chemical Oscillations, Waves and Turbulence, Springer-Verlag, 1984.
[30] P. Coullet, J. Lega, B. Houchmanzadeh, L. Lajzerowicz, Phys. Rev. Lett. 65 (1990) 640.
[31] T. Kawagishi, T. Mizuguchi, M. Sano, Phys. Rev. Lett. 75 (1995) 3768.
[32] P.G. de Gennes, J. Prost, The Physics of Liquid Crystals, 2nd ed., Oxford Science Publications/Clarendon Press, 1993.
[33] V. Fréedericksz, V. Zolina, Trans. Faraday Soc. 29 (1933) 919.
[34] M.O. Cáceres, F. Sagués, M. San Miguel, Phys. Rev. A 41 (1990) 6852.
[35] J.D. Murray, Mathematical Biology, Springer-Verlag, Berlin, 1993.
[36] G. D'Alessandro, W.J. Firth, Phys. Rev. A 46 (1992) 537.

[37] E. Pampaloni, S. Residori, F.T. Arecchi, Europhys. Lett. 24 (1993) 647.
[38] B.A. Samson, M.A. Vorontsov, Phys. Rev. A 56 (1997) 1621.
[39] Y. Pomeau, Physica D 23 (1986) 3.
[40] R.A. Fisher, Ann. Eugenics 7 (1937) 335.
[41] A. Kolmogorov, I. Petrovsky, Piskunov, Bull. Univ. Moskou Ser. Int. Se. 7 6 (1937) 1.
[42] D.G. Aronson, H.F. Weinberger, Adv. Math. 30 (1978) 33.
[43] P. Coullet, C. Riera, C. Tresser, Phys. Rev. Lett. 84 (2000) 3069.
[44] E. Pampaloni, P.L. Ramazza, S. Residori, F.T. Arecchi, Phys. Rev. Lett. 74 (1995) 259.
[45] M.G. Clerc, R. Rojas, A. Petrossian, S. Residori, preprint 2003.